AIMS Materials Science, 9(2): 236–254.
DOI: 10.3934/matersci.2022014
Received: 15 November 2021
Revised: 30 January 2022
Accepted: 17 February 2022
Published: 22 February 2022

http://www.aimspress.com/journal/Materials

*Research article*

# Heat input effects on mechanical constraints and microstructural constituents of MAG and laser 316L austenitic stainless-steel welded joints

**Francois Njock Bayock[1,*], Paul Kah[2] and Kibong Marius Tony[3]**

[1] Department of Mechanical Engineering, ENSET Douala, University of Douala, P.O. Box: 1872, Douala, Cameroon
[2] Department of Engineering Science, University West, Gustava Melius gata 2 S-461 32 Trollhättan, Sweden
[3] Laboratory of Technologies and Applied Sciences, University Institute of Technology, University of Douala, PO Box 8698 Douala, Cameroon

* **Correspondence:** Email: njockfm1@outlook.com; Tel: +237 681 559 539.

**Abstract:** This study aims to investigate the optimum heat input required to overcome the negative consequence of the thermal properties of austenitic stainless steel to produce welded joints free of distortion. An experimental investigation using robotic-MAG and fiber-laser welding processes has been used in other to investigate angular, longitudinal distortion (bending), and microstructural constituents in the heat-affected zone (HAZ) of different welded joints. Ten 316L steel, butt-joints were made by different travel 25 speeds at the range of (7–11 mm/s). A highly sensitive 2D-laser device has been used to measure the distortion then, a microstructural investigation was done using an optical micrograph, Scanning Electron Microscopy (SEM) coupled with the Electron Dispersive Spectrometer (EDS). The laser-fiber welding process results indicated optimum parameters to prevent distortion when applying welding speed of 2.2 m/min, the power source of 2.5 kW, and the focal position of 3 mm. In MAG welding, test results revealed an increase of longitudinal distortion (bending) from 1.2 mm to 3.6 mm when raising the heat input from 0.3 to 0.472 kJ/mm. When increases welding speed (11 mm/s), angular distortion was approximately 2.1° on the left side and 1.7° on the right side. Microstructural investigations revealed the proportionality between heat input and carbides formations on the grain boundaries of HAZ. They were also the formation of etching pores and some ferrite content (10%) on the weld center.

**Keywords:** heat input; angular distortion; hot cracking; microstructural constituent longitudinal distortion; 316L stainless steel; SEM; EDS microscopy

## 1. Introduction

Stainless steel is the prevailing material in many industries due to its strength, ductility, and corrosion resistance. The production of stainless steel has increased from five million tons in 1970 to forty-eight million tons in 2017 [1]. The oil and gas industry, automotive manufacturing, household utensils, chemical plants in addition to the offshore and highly corrosive environment are the dominant consumers of stainless steel [2]. More than half of the stainless-steel-produced parts are a cold-rolled sheet, about one-fifth are bars, and 10% are hot rolled plates. Stainless steel tubes are common in production and casting is minor. Almost 25% of stainless-steel production serves the food industry sector, 20% for chemical, oil, and gas industry, 8% for washing machines, and the same amount for transportation. Frying pans and cutlery represent 9% of the total production of stainless steel and 5% for each construction sector, pulp, and paper industry. Energy and kitchen equipment besides other applications form the remaining percentage [2]. Stainless steel is an excellent material for fire resistance, even in case of fire it is a safe material, it does not emit any toxic fumes. Therefore, it is favorable material for many applications inside buildings such as stairways, floor coating besides walls, and tunnel cladding [3].

Austenitic stainless steel is the leading group of stainless steel due to the wide range of applications [3–5]. Austenitic stainless steel is a non-magnetic material, produced in a solution-annealed state; heat treatments are not applicable for hardening the material [6]. Austenitic stainless steel is an ideal selection to resist many corrosive environments. Moreover, it guarantees the required ductility for cryogenic temperatures applications. However, distortion is a common defect in welding of the austenitic stainless steel, wherein the shipbuilding industry; 20–30% of the weight of labor job is reworking due to the welding distortion [7]. Distortion leads to the reduction of fatigue strength and minimization in the load capacity of the welded structures [8–10]. The high thermal expansion coefficient of austenitic stainless steel is responsible for the distortion as a result of the relatively high heat introduced during the arc welding process [11–16]. This problem can be minimized by using lower heat input welding techniques such as laser welding [6–13]. Additionally, when welding there is a risk when welding 316L austenite stainless steel, which is the formation of crack propagations (hot cracks) and intergranular corrosion in the weld or HAZ [17,18]. The increase in the brittleness of welds by applying higher temperature can be the result of the appearance of some sulfur, phosphorus causing porosity and intergranular corrosion [19,20].

Ramkumar et al. [21] investigated the influence of different filler metals on the microstructure, mechanical properties, and corrosion resistance of AISI 316L (X2CrNiMo17-12-2). Pulsed current tungsten inert gas has been adopted as the primary welding process for the experiment. Charpy- V notch and tensile tests were carried out to examine the mechanical properties after welding. A close relationship between the applied filler metal against the mechanical and physical properties of the welded joint has been proved [16]. Shankar et al. [22] investigated the effect of the shielding gas additives on the weldability of austenitic stainless steel 316L (X2CrNiMo17-12-2) and 316LN (X2CrNiMoN17-11-2). They manipulated the amount of nitrogen in the shielding gas within the range (0.04–0.19%). A longitudinal moving torch Varestraint test has been applied to evaluate the

weldability. The study revealed the relationship between the impurity level and cracked probability in presence of nitrogen. Younes et al. [23] carried out mechanical examinations to compare the strength of 304L stainless steel (X2CrNi19-11) welded by TIG and other samples joined with the electron beam (EB). Moreover, Younes et al., have exposed the tensile specimens to hydrogen gas to observe the effects of the different amounts of $H_2$ gas on the mechanical properties. Hydrogen addition has improved the tensile strength and yield strength. However, it has reduced the ductility; it also changed the fracture mode and initiated cracks near the austenite-ferrite interface. Hydrogen embrittlement was found to be higher with TIG process.

This study aims to investigate the weldability of austenitic stainless steel in terms of the tendency to geometrical deformation and microstructural constituents in the HAZ caused by the different welding processes. The study has followed an experimental procedure to reveal and measure angular and longitudinal distortion in square, butt-joints of 316L stainless steel. The study aims to answer the question; how much is the optimum heat input produced by an electrical arc welding process to mitigate distortion and achieve soundness in the welded joint? The study investigated the effects of the mechanical constraints in preventing longitudinal and angular distortion. The effect of different welding processes on the microstructural constituent of the HAZ was also investigated in this research work.

## 2. Materials and methods

Robotic gas metal arc welding (GMAW) and continuous wave (CW) laser welding processes were applied to produce ten squares (I joint), butt-joints. Base material (BM) is low carbon-austenitic stainless steel 316L (1.4404), filler material for the GMAW process is "Elga Cromamig 316L Si" with similar properties to the parent material. Tables 1 and 2 show the chemical composition and the mechanical properties of the BM and filler material, respectively.

The adopted air gap is 1.2 mm, and the plate's dimensions are 100 mm × 200 mm × 3 mm. Shielding gas (98% Ar + 2% $CO_2$) is a combination of argon (Ar) and carbon dioxide ($CO_2$) to ensure arc stability, control the spatters and guarantee the required penetration [24–26]. Different heat inputs per unit length (kJ/mm) were applied by employing variable welding speeds. The objective of the experimental work is to investigate the effect of the welding process and the applied heat input on the welding quality of 316L stainless steel. Distortion, hot cracking, different σ-phase transformations in the HAZ have been investigated within the scope of this study.

**Table 1.** Material's chemical composition (wt%).

| Material | C | Si | Mn | P | S | Cr | Ni | Mo | N |
|---|---|---|---|---|---|---|---|---|---|
| 316L austenitic stainless-steel | 0.018 | 0.45 | 0.98 | 0.038 | 0.001 | 17.1 | 10.0 | 2.04 | 0.036 |
| Filler wire | 0.015 | 0.80 | 1.70 | 0.015 | 0.01 | 18.0 | 12.0 | 2.60 | 0.060 |

**Table 2.** Mechanical properties of the BM and filler material.

| Material | Yield strength (Rp), MPa | Tensile strength (Rm), MPa | Elongation A5 (%) | Hardness HV5 |
|---|---|---|---|---|
| 316L austenitic stainless-steel | 317 | 603 | 56 | 182 |
| Filler wire | 350 | 520 | 30 | - |

For the robotic-MAG welding samples (6 samples), full constraints were applied for three of them to investigate the influence of the mechanical clamps on the produced distortion. The rest of the samples (3 samples) have been welded after a partial fixing. Figure 1 shows the different types of applied fixing for the robotic-MAG samples.

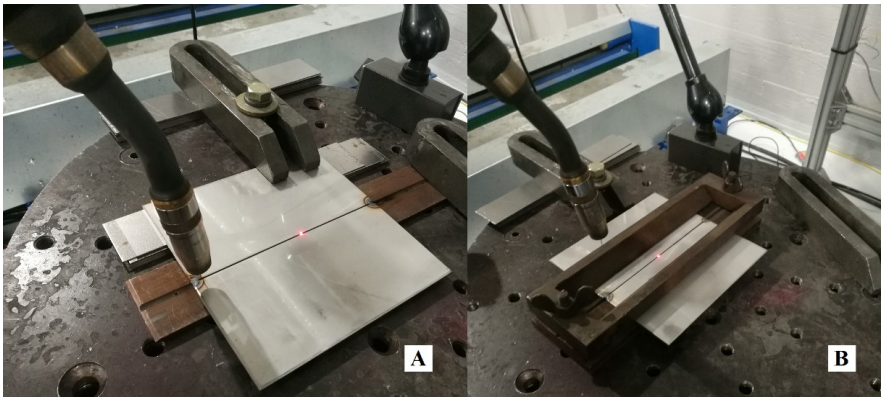


**Figure 1.** Welding fit-up, partial fixing (A), and full constraints (B).

Welding current and voltage were maintained constant for all samples, while welding speed was varied. Tack welding was applied with TIG to ensure a uniform air gap. Eq 1 to calculate the heat input per unit length for the MAG welding, as per the (EN 1011-1).

$$Q = \frac{K \cdot V \cdot I}{\nu \cdot 1000} \tag{1}$$

Where $Q$ represents the heat input per unit length (kJ/mm), $K$ is the thermal efficiency which is 0.8 for GMAW, $V$ is voltage (V), I represent the welding current (A) and ν is the welding speed (mm/s). For the heat input calculations of the laser welding, Eq 2 was applied.

$$Q_L = \frac{K \cdot P \cdot 60}{\nu \cdot 1000} \tag{2}$$

$Q_L$ represents the heat input per unit length out of the laser source (kJ/cm), P is the laser power (kW), thermal efficiency (K) is 0.9, and ν is the laser speed (m/min). Table 3 presents the welding parameters for the laser-welded samples and it can be seen different values of heat input, laser power, speed, and local position. Table 4 presents the welding parameters for the robotic-MAG welding process.

**Table 3.** Laser welding parameters.

| Sample | Power (kW) | Travel speed (mm/min) | Focal length (mm) | Heat input (kJ/mm) |
|---|---|---|---|---|
| Laser-1 | 4 | 30 | 30 | 0.072 |
| Laser-2 | 3 | 25 | 30 | 0.065 |
| Laser-3 | 2.5 | 22 | 30 | 0.061 |
| Laser-4 | 2 | 20 | 00 | 0.054 |

**Table 4.** Welding parameters for the robotic-MAG samples: PF = Partial fixing; FC = Full constraint.

| Sample | Filler metal (mm) | Welding current (A) | Arc voltage (V) | Travel speed (mm/s) | Wire feed rate (m/min) | Heat input values (kJ/mm) | Run-out length (mm) | Remarks |
|---|---|---|---|---|---|---|---|---|
| MAG-1 | 1.0 | 160 | 25 | 9.0 | 9.5 | 0.355 | 18 | PF |
| MAG-2 | 1.0 | 157 | 26.3 | 7.0 | 9.5 | 0.47 | 18 | PF |
| MAG-3 | 1.0 | 157 | 26.3 | 11.0 | 9.5 | 0.30 | 18 | PF |
| MAG-4 | 1.0 | 157 | 26.3 | 9.0 | 9.5 | 0.36 | 18 | FC |
| MAG-5 | 1.0 | 155 | 26.4 | 7.0 | 9.5 | 0.46 | 18 | FC |
| MAG-6 | 1.0 | 157 | 25.4 | 11.0 | 9.5 | 0.29 | 18 | FC |

### *2.1. Angular distortion measurement*

A sensitive laser-2D device was used to measure the angular distortion on the welded joints. The measuring system consists of a laser source fixed to a rectangular beam that can move in two perpendicular directions. The measuring device is associated with software to collect the data from the laser sensor. The software draws a mirror image for the plate in the direction of the measurement; the data from the software can be transferred and treated by another program such as Microsoft Excel for further analysis. The measuring device was calibrated before the experiment to set the zero points (height in Y direction and length in the X direction). The measuring device is highly sensitive, where it hits hundreds of height (Y) readings in one single location. Angular distortion values were measured at three (3) positions on each welded sample, both ends, in addition to the center of the plate named T1, T2 and T3, as shown in Figure 3. Readings were obtained by moving the laser beam source manually through the fixed beam to pass along the T1 line that is drawn on the welded plate. The obtained readings (height and length) were transferred to the excel file to plot the geometry of the welded plate and measure the deviation from the right axes (distortion). The same procedure was repeated on the T2 and T3 lines; then, the maximum value of distortion among the three lines was considered. Figure 2 presents the laser 2-D device utilized in measuring the angular distortion on the welded plates, and the graph shows the lineation (T1, T2, and T3) on the surface of the plates created to facilitate the measuring process.

Figure 2 presents the measuring setup of the welding sample (1), four cylindrical supports (2) were calibrated to ensure the same height for each, the laser sensor (3), and the movable beam (4) are used to run the laser source through the measuring lines (T1, T2, and T3). The data from the measuring device software obtained in notepad file format then transferred to excel files and then, a mirror image of the plate profile at T1, T2, and T3 have been drawn. Therefore, the angular distortion calculations were done based on Eq 3.

$$\theta = Tan^{-1} Y/X \tag{3}$$

Where $\Theta$ is the angular distortion in deg, $Y$ vertical displacement in mm at the end of the measurement line deviated from the original location (0) before welding. $X$ is the transverse displacement in mm from the weld center to the end of the line (TI, T2, or T3). The distortion angle was measured on both ends.

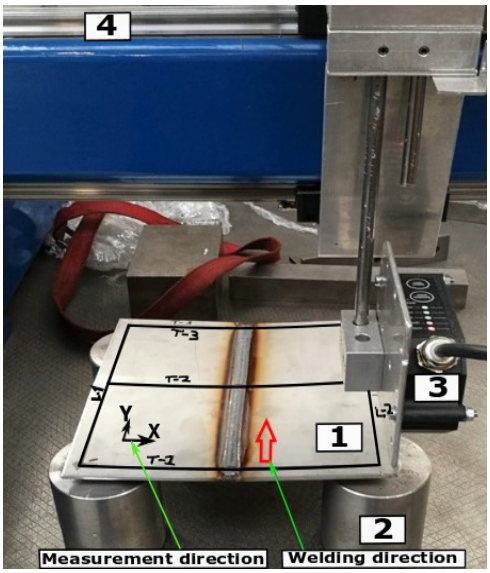


**Figure 2.** The laser-2D device, was utilized for measuring distortion.

*2.2. Longitudinal distortion (bending) measurements*

The same device and mechanism applied for measuring angular distortion were adopted for longitudinal distortion. The maximum height deviation from the original position of the plate (straight) represents the magnitude of the longitudinal distortion. Figure 3 shows the maximum value of the longitudinal distortion or bending which can be found at the center of the plate (A) or any other position along the length of the plate (B), the length (x) represents the magnitude of the longitudinal distortion (mm).

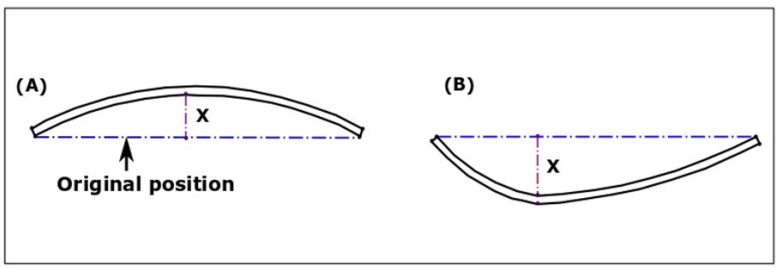


**Figure 3.** Longitudinal distortion measurements show: (A) longitudinal distortion at the center; (B) longitudinal distortion at any position along the length of the plate.

*2.3. Macro/micro examinations, SEM and EDS investigation*

The metallographic samples were prepared through several steps, starting with dry grinding, wet grinding, polishing, etching in 10% oxalic acid diluted in water in the presence of an electrolyte, and finally, samples were dipped in the water-alcohol solution. The obtained micrographs were utilized to assess the quality of the welded joints at the macro level, by applying the acceptance criteria and quality evaluation as per EN ISO 5817. Then, microscopic examination was used to check the phase

transformation due to the applied heat. Carbides formation was targeted as well through the microstructure investigation. Chromium carbides precipitation on the grain boundaries in HAZ is a common phenomenon in austenitic stainless steels [27–29], where chromium tends to connect with carbon at specific temperatures, then accumulates at the grain boundaries, and chromium depleted from the area adjacent to the carbides accumulations which may increase the risk of Intergranular corrosion (IGC). Optical microscopy with different magnifications was used to reveal the welded samples' microstructure. MAG-2, MAG-3, and laser-3 samples were investigated with SEM and EDS mapping tests to study the effects of the heat input on the microstructural constituent of 316L stainless steel HAZ. The selected samples represent the maximum and minimum heat input and cover both welding processes.

## 3. Results and discussion

Welded plate coordinates obtained from the laser 2D device have been analyzed and transferred into deformation data utilizing simple calculations on an excel sheet. The analysis of the angular distortion was performed based on the deformation on the front side of the plates (T1), where the welding started. While longitudinal distortion has been considered on the plate side with the higher deformation (L1).

### *3.1. Angular distortion results*

As discussed in 3.1, the data from the laser device software were obtained and treated in an excel sheet to plot a mirror image for the welded plates in the direction of the angular distortion. Figure 4 shows the angular distortion for the MAG welded plates; it shows the name of the sample. Welding speed and the calculated distortion angle as per Eq 3 can be read from the figure caption.

It can be extrapolated from the distortion sketches that angular distortion has increased slightly when the welding speed is reduced from 9 to 7 mm/s. When the welding speed increased to 11 mm/s, angular distortion was significantly minimized to less than 1° at both sides of the plate. A slight increase of the travel speed than the value applied for MAG-3 can produce a welded joint free of distortion.

It can be noticed as well from the Figure above that, constraints do not mitigate the angular deformation on the 316L plate. However, the direction of the angular distortion has reversed, and the magnitude of the distortion angle decreased slightly. Figure 5 shows the distortion of the laser-welded samples. The welding parameters can be seen in the same figure. Angular distortion is relatively less when compared to MAG welding.

Laser welding parameters applied to the sample (laser-1) have produced a weld joint almost free of distortion. A very small amount of angular distortion has been observed on laser-1 plate, which indicates the reverse-proportional relation between the welding speed and the produced angular distortion. Nevertheless, full penetration has not been achieved. Lack of penetration (LOP) has been observed in laser-2 samples as well. Laser-3 sample has shown an optimum overall quality among the other laser samples in terms of distortion angle and penetration. Nevertheless, it shows a little amount of spatter. Spatter has been reduced in laser-4 sample by changing the focal position from 3 mm to 0. It can be observed that laser-3 sample shows a better distortion compared to laser-2. However, the welding speed was less. This can be justified by the lower laser power in laser-3.

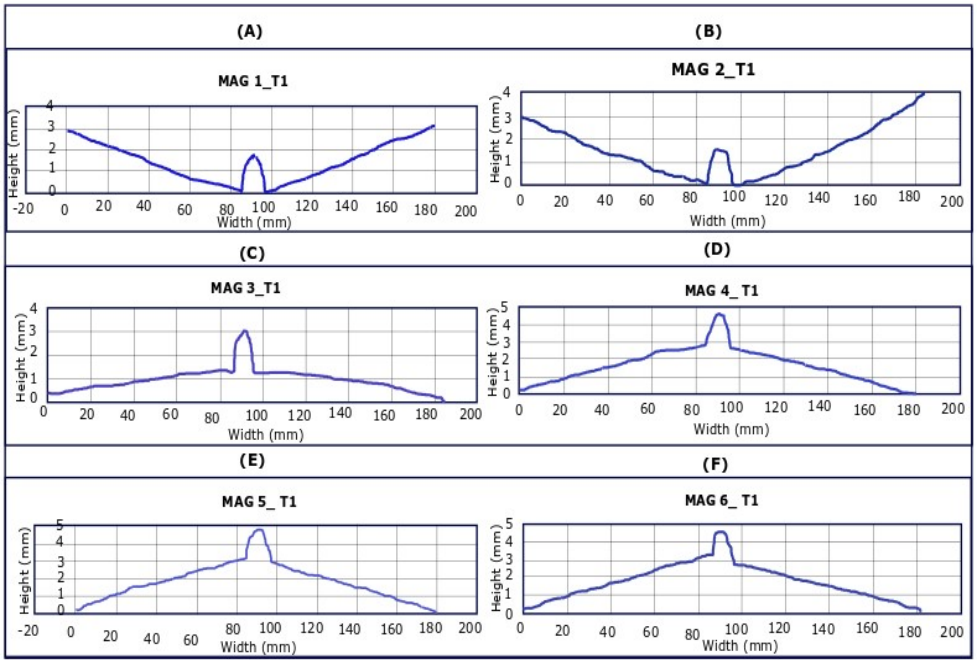


**Figure 4.** Angular distortion in MAG welded samples, for (A) welding speed is 9 mm/s, distortion angle is 2.3°. (B) Welding speed is 7 mm/s, distortion angle 2.2° on the left side, and 2.5° on the right side. (C) Welding speed is 11 mm/s, angle of distortion is 0.9°. (D) Welding speed is 9 mm/s-welding under full constraint, and the distortion angle is 1.9° on the left side and 1.7° on the right side. (E) Welding speed is 7 mm/s and distortion angle 2°. (F) Welding speed is 11 mm/s, angle of distortion is 2.1° on the left side and 1.7° on the right side.

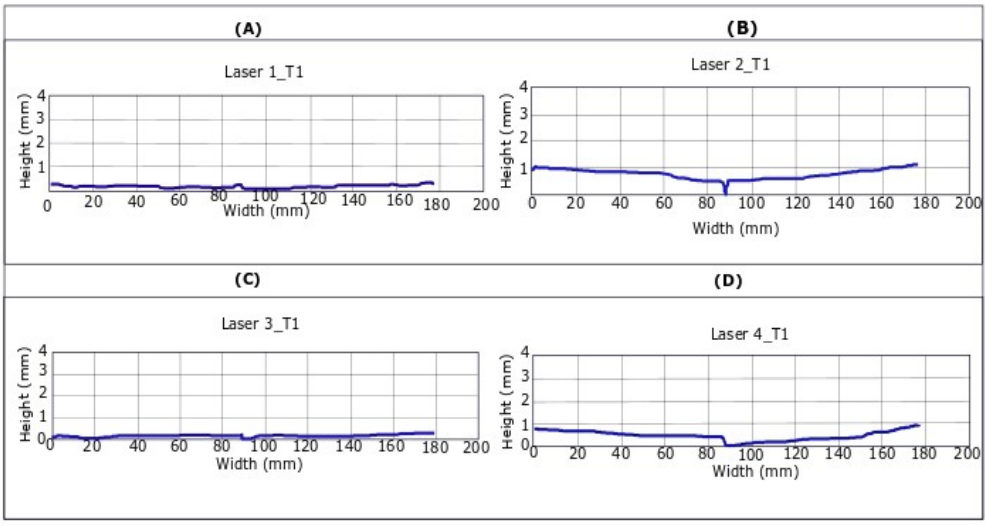


**Figure 5.** Angular distortion for the laser-welded samples. Laser welding parameters for (A) are 4 kW, 3 m/min, and 3 mm for the laser power, welding speed, and focal length, respectively, and the calculated distortion angle is 0.1°. (B) 3kW, 2.5 m/min, and 3 mm. The distortion angle is 0.8°. (C) 2.5 kW, 2.2 m/min, and 3 mm. the angle of distortion is 0.1°. (D) 2 kW, 2 m/min, and 0 mm. the angle of distortion is 0.7°.

Figure 6 shows the relation between the welding speed, heat input, and the produced angular distortion for the MAG welded samples. It found that welding speed and angular distortion are reversely proportional to each other for the free ends joint. While for the constrained plates, distortion increases slightly when welding speed is raised to a specific limit then remains constant and independent from the speed. Concerning the heat input into the weld seam, angular distortion is always greater with a higher amount of heat input when no constraints are applied. However, for the constrained plates, angular distortion begins to increase with the higher heat input per unit length then decreases after a certain limit. It can be seen from the Figure that, applying the mechanical clamps to fix the welded plates before the welding process does not prevent the occurrence of distortion. For example, by applying welding speed of 11 mm/s, the plate distorts towards the opposite direction in comparison to the slower speeds. However, the magnitude of angular distortion is different from the fully constrained joints.

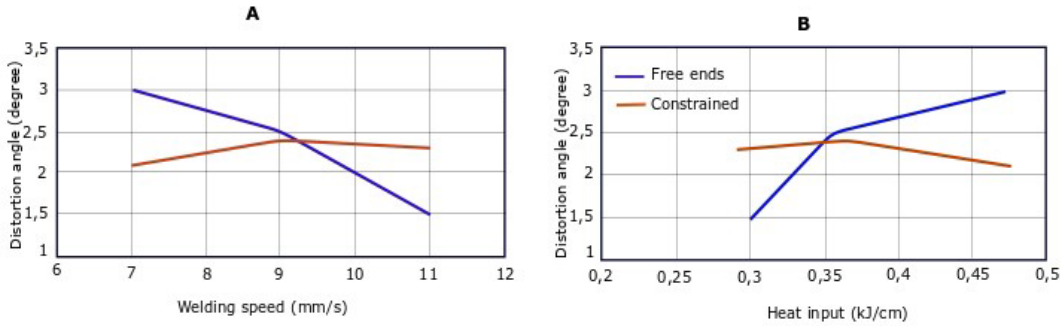


**Figure 6.** The relation between angular distortion and welding speed (A). The relation between heat input and angular distortion (B).

*3.2. Longitudinal distortion (bending) results*

Figure 7 presents the longitudinal distortion on the MAG and laser-welded plates. It can be seen that 316L tends to bend when welded with MAG while it keeps the original geometry when joined with laser welding. For free-end joints, longitudinal distortion increases when welding speed decreases, and the lowest value of angular distortion happened at the highest welding speed, which is 11 mm/s in MAG-3 sample, and the bending direction was opposite to the direction in the other samples where the welding speeds were lower. Constraints have failed to restrict the longitudinal distortion; rather, it reverses the direction of bending. Welding speed has minimal effects on the magnitude of distortion when the joint is constrained. The Laser-3 sample again showed the optimum results.

Figure 8 shows the relation between the welding speed, heat input, and the produced longitudinal distortion for the MAG welded samples. It is shown that welding speed and angular distortion are proportional to each other when applying Free ends Joint. By applying for the constraint plates, the results show a slight increase of distortion when welding speed is raised to a certain limit. After that, there is the distortion remains constant and independent from the speed. Based on the relation between heat input and angle distortion on the weld joints, there is always an increase of angular distortion when applying higher heat input especially when no constraints are applied. In Figure 8, the results indicated that when applying the mechanical clamps to fix the welded plates

during the welding process, there is no prevention of the occurrence of distortion of welded samples. However, the application of full constrained joints can be the result of a difference of magnitude of angular distortion.

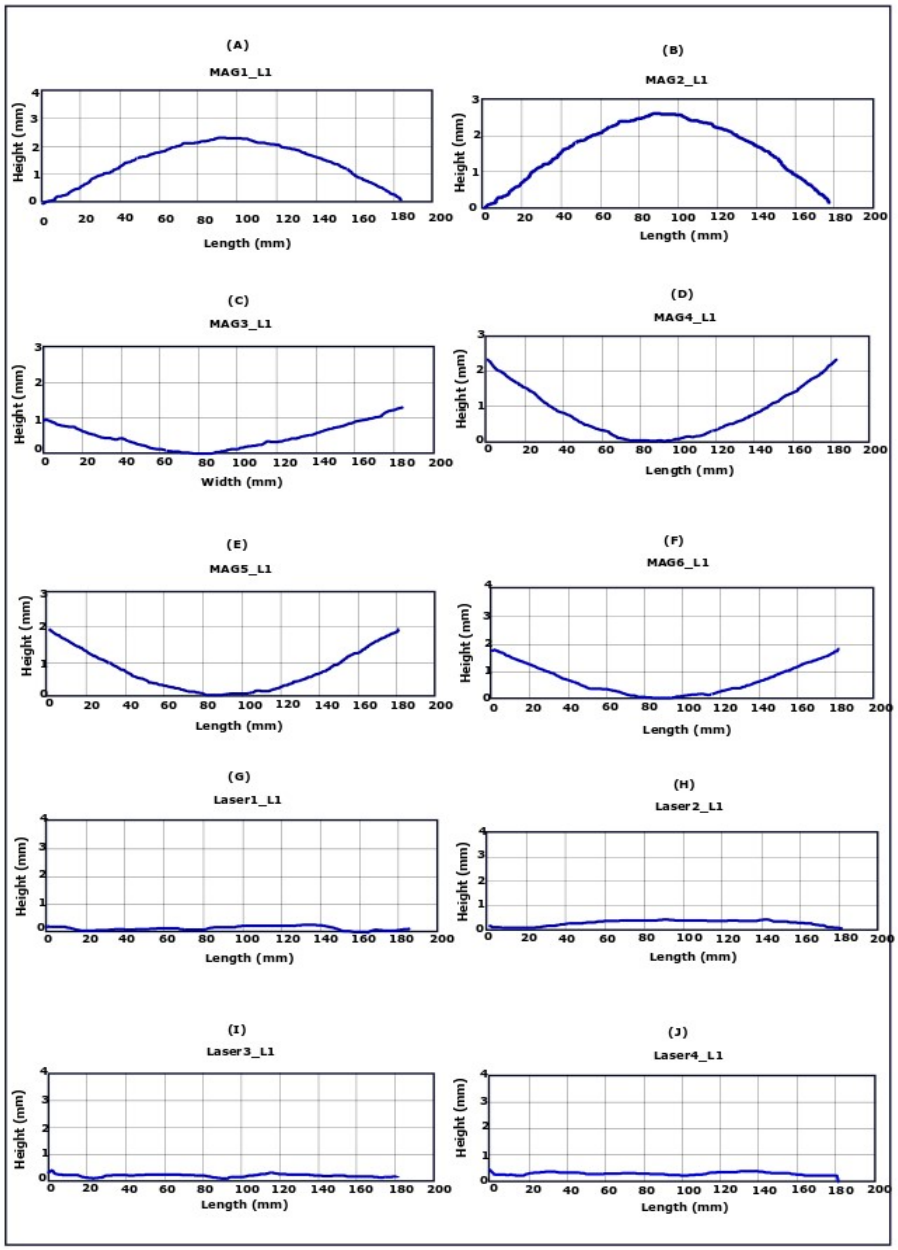


**Figure 7.** Longitudinal distortion for the weld samples, 2.2 mm, 2.58 mm, 1.23 mm, 2.2 mm, 1.9 mm, 1.7 mm, 0, 0.34 mm, 0, and 0.27 mm for A, B, C, D, E, F, G, H, I and J respectively.

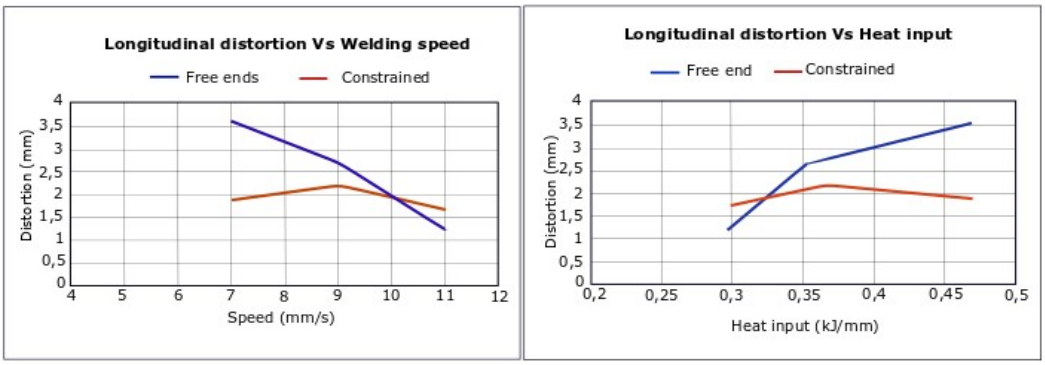


**Figure 8.** The relation between longitudinal distortion, welding speed, and heat input.

### *3.3. Microstructure analysis and hot cracking*

The presence of the ferrite phase is advantageous to mitigate hot cracking in austenitic stainless steel, while 100%-austenite microstructure is more sensitive to fissuring at elevated temperatures. The ferrite phase prevents the segregation of low-melting elements such as phosphorus and sulfur, therefore, reducing the probability of hot cracks. On the other hand, the high level of the delta-ferrite phase reduces the corrosion resistivity of austenitic stainless steel [29]. Ferrite content as a percentage of welded austenitic stainless steel can either be measured utilizing special devices such as Feritoscope or predicted by employing Schaeffler-diagram for the MAG welding samples. Figure 9 represents the filler metal and the base metal position on Schaeffler-diagram based on calculated Creq and Nieq.

Considering the dilution of 50%, Creq/Nieq is 1.7, which indicates the presence of the δ-Ferrite phase [30,31]. Figure 9 shows an Austenite-Ferrite (AF) Solidification mode, a content of 5% ferrite approximately is present in the structure of the welded joints, which indicates an excellent resistance for hot cracking and a possible tendency for intergranular corrosion (IGC)

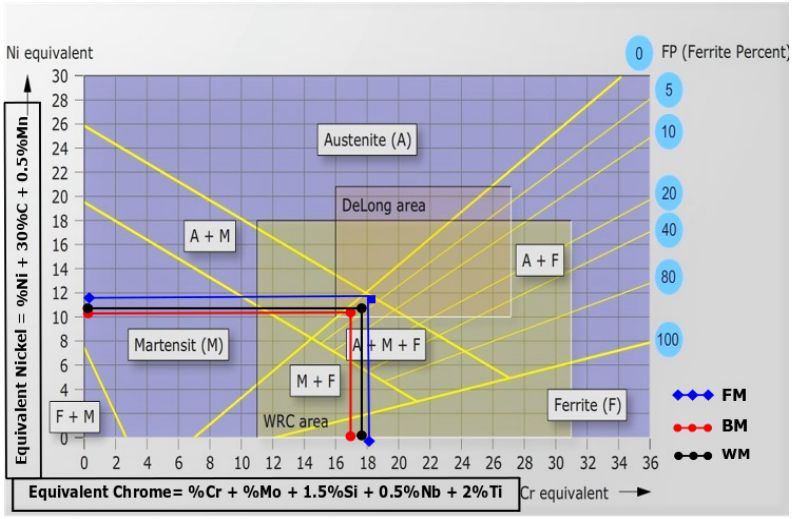


**Figure 9.** Schaeffler diagram for 316L and filler material showing the BM and FM (Elga cromaning 316L Si).

Figures 10 and 11 present the obtained microstructure images for the welded samples taken by the optical microscopy at the fusion line and weld center respectively. As discussed earlier, the solidification mode was AF. Therefore, most of δ-ferrite has transformed into austenite (γ) at room temperature. While a tiny percentage of δ-ferrite has remained after solidification, it can be seen with dark streaks on the grain boundaries of HAZ in Figure 10. Figure 11 shows the etching pores produced during the sample preparation process. A centerline crack is suspected in sample laser-2 due to the relatively high welding speed, while the welding speed in laser-1 sample was higher, other parameters such as laser power might be affected by the occurrence of the centerline crack. As shown by Figure 10, a grain coarsening took place in the HAZ as well. Similar results have also been reported for gas metal arc welded austenitic and ferrite stainless steel plates in which a coarse-grained structure existed within the HAZ region and the grain coarsening increased by the increase in heat input [3,4].

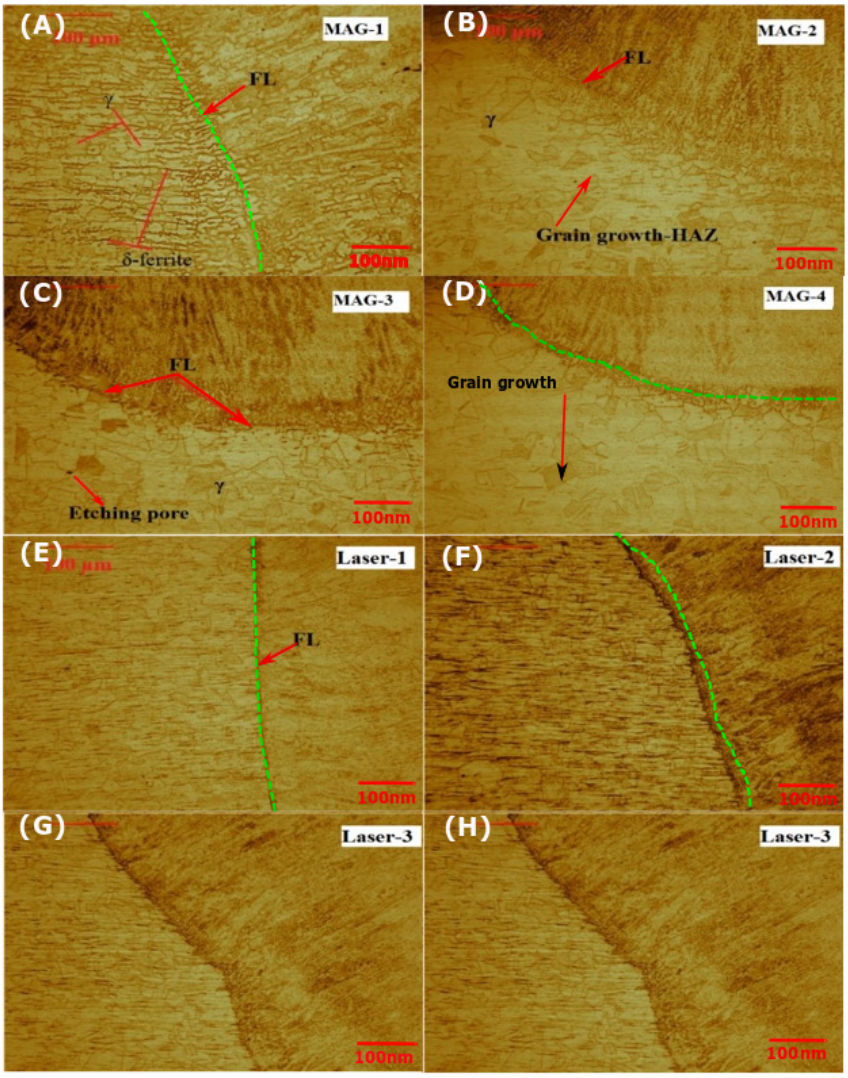


**Figure 10.** Optical microscopy images for welded samples at the fusion line.

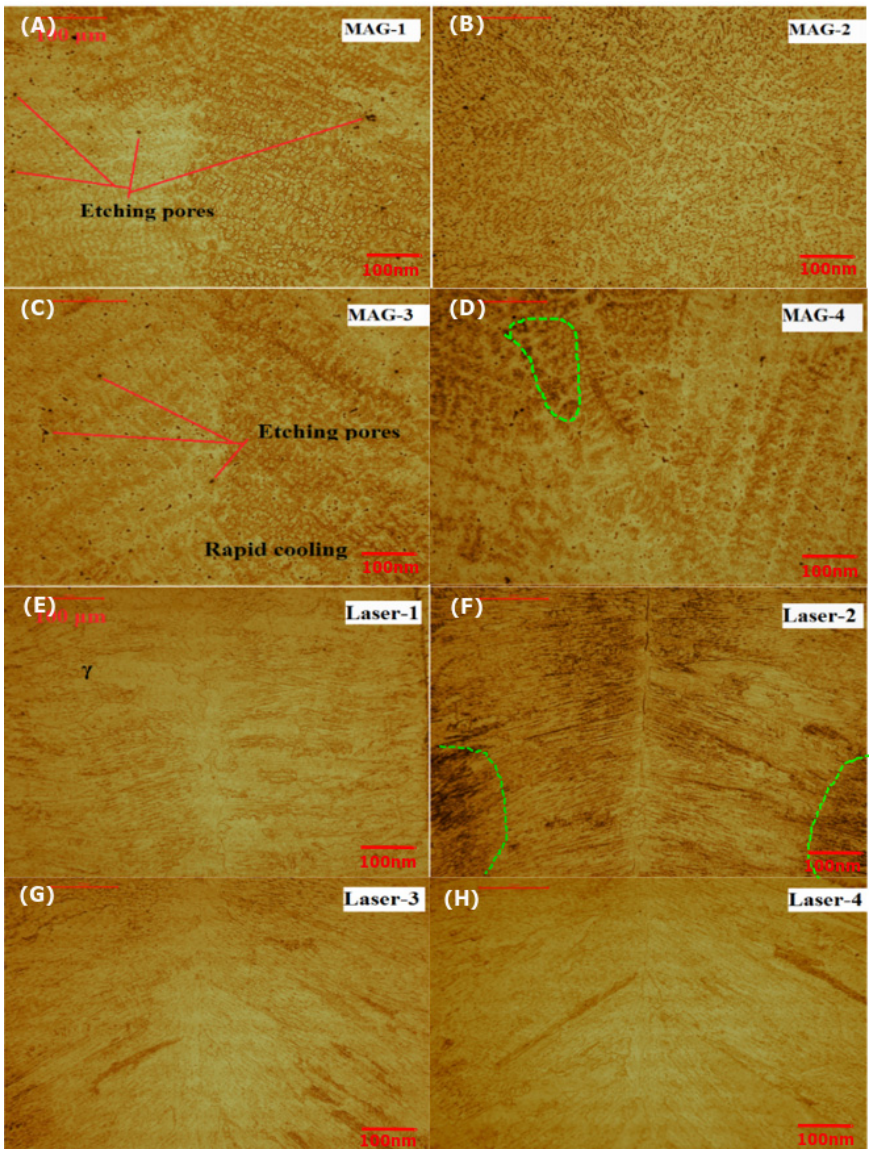


**Figure 11.** Optical microscopy images for welded samples at the weld center.

*3.4. SEM, EDS, results*

Two MAG samples; MAG-2 and MAG-3 with the lowest and highest welding speed; 7 mm/s and 11 mm/s respectively were tested in SEM device in addition to one laser sample (laser-3). Figure 12 presents the obtained SEM images for the samples at the fusion line and weld center. The dominant austenite phase is observed in addition to the residual δ-ferrite on the grain boundaries of the coarse grain area- HAZ at the vicinity of the fusion line. SEM investigation has revealed a clear indication for carbide formation at an area of HAZ close to the fusion line. Carbides precipitation at the base metal area is rarely occurs due to the permanent homogeneous structure in terms of chromium diffusion [21]. The visibility of the indication in MAG-2 sample was superior to it in MAG-3. Figure 13 shows the observed indication by SEM in the form of white accumulations on the grain boundaries.

The nature of these indications has been investigated by applying the EDS inspection. Cr atoms

that participated in the formation of precipitates had diffused from austenite grains, which exist adjacent to the noncoherent interface between the grains boundaries and the matrix as a result of the applied energy during welding and the dwell time when the temperature was about 650 ℃. Accordingly, Cr depletion takes place in the microstructure, which may enhance the IGC in the future [15].

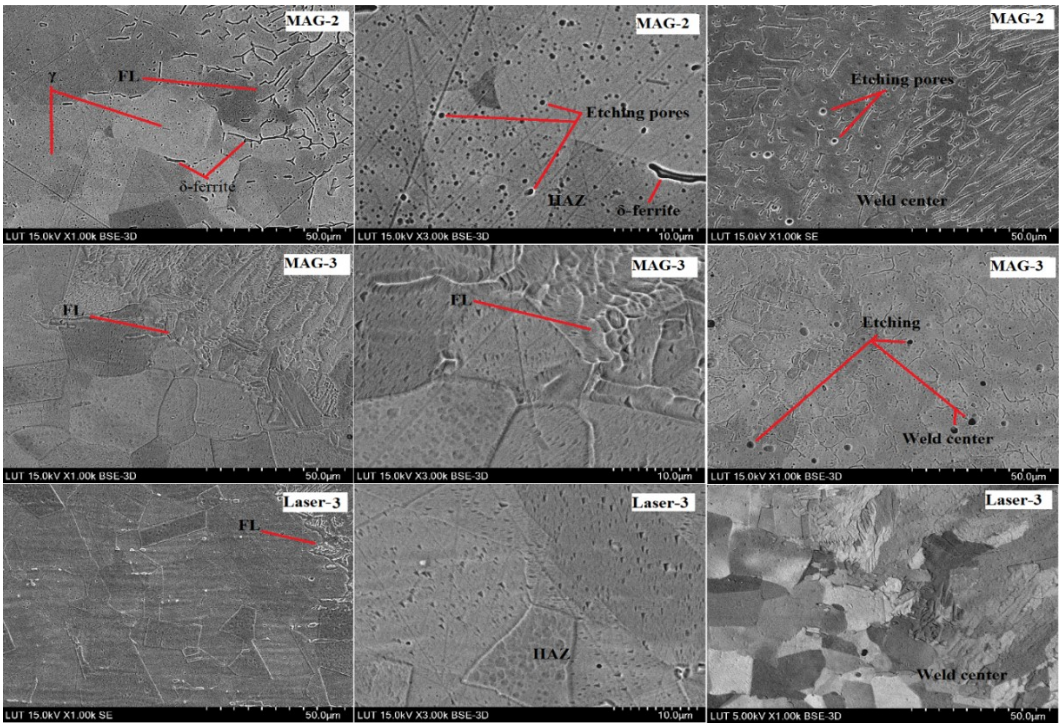


**Figure 12.** SEM-microstructure images for welded samples MAG-2, MAG-3 and Laser-3.

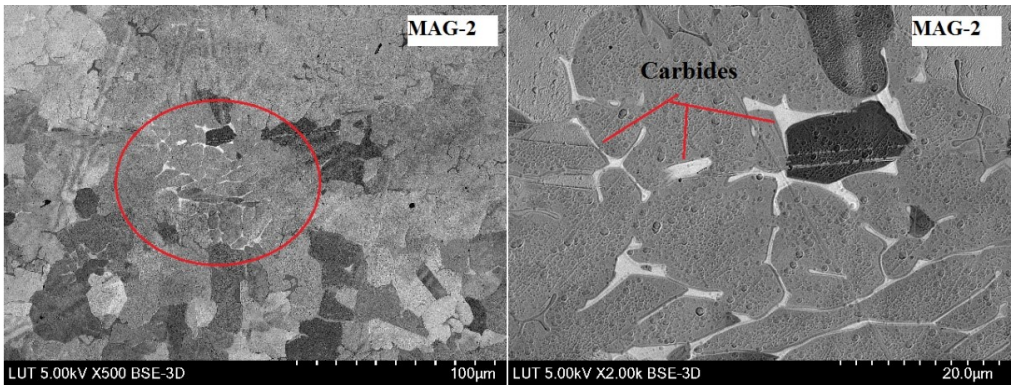


**Figure 13.** Carbides formation indication.

Figures 14 and 15 show the EDS scan for the welded samples MAG-2 and MAG-3, respectively. It can be seen from the EDS images that chromium and molybdenum concentration has increased at the area of indication while nickel content has decreased. At the scanned area, chromium percentage jumped to 26% while the original weight of chromium in the base metal was 17%, molybdenum as

well increased from 2% to 5.6%. At the same time, nickel has depleted from 10% to 2–4%, which indicates the formation of mixed carbides between C, Cr, and Mo. No change in carbon content can be observed due to the tiny percentage of carbon in 316L [32,33]. The same result has been observed for MAG-3 sample. However, the concentration of the carbides was less compared to MAG-2, which indicates the effects of heat input on the σ-phase transformation including potential carbide precipitation as well.

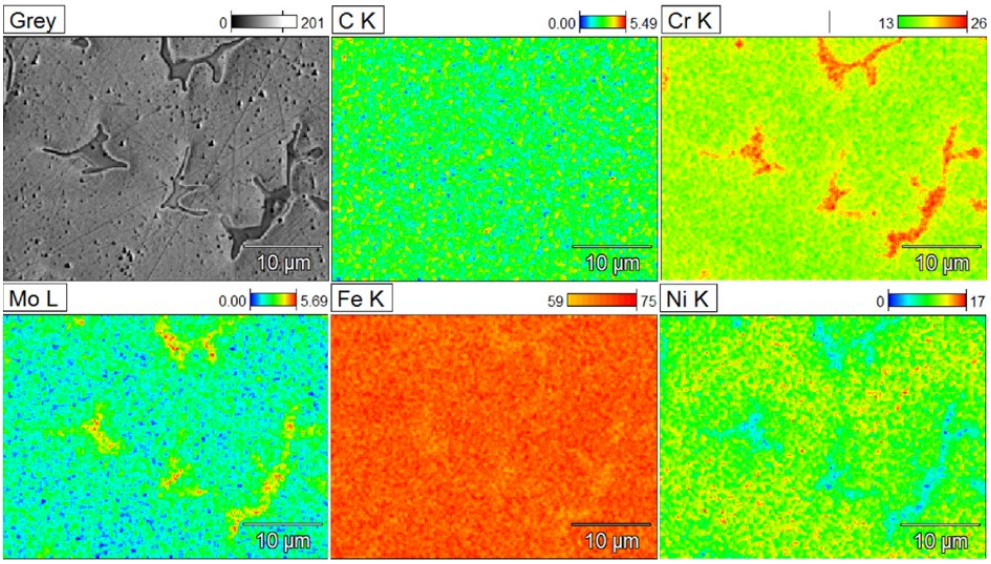


**Figure 14.** EDS mapping scan for sample MAG-2 at HAZ-Carbides formation.

Though the presence of the precipitates on the grain boundaries, the probability of the sensitization occurrence is too low due to the small amount of carbon content in both filler material and base metal in addition to the short dwell time in the sensitization range. Similar results can be justified when analyzing the concentration gradient of alloying elements (Fe, Cr, C, Mo, Ni) on the coarse grain heat-affected zone of 316L austenitic stainless steel [34].

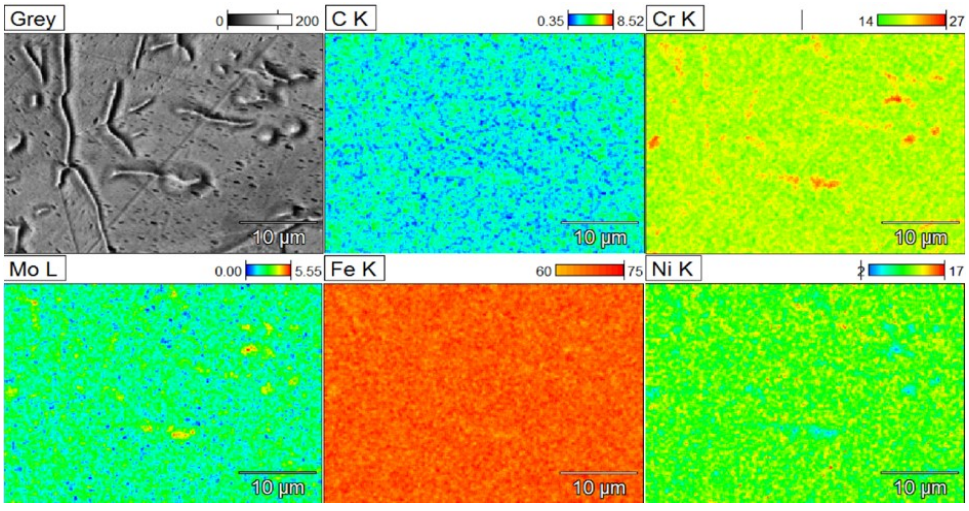


**Figure 15.** EDS mapping scan for sample MAG-3 at HAZ-Carbides formation.

## 4. Conclusions

Distortion is a real concern for welded structures due to the negative consequences associated with it. In this study, the influence of the heat input, welding process, and mechanical constraints on the angular, longitudinal distortion, and microstructural constituents of 316L austenitic stainless steel welded joint has been investigated. Based on the experimental analysis, the following findings were shown.

- The laser-fiber welding process results indicated optimum parameters to prevent distortion when applying welding speed of 2.2 m/min, a power source of 2.5 kW, and a focal position of 3 mm.
- When increased welding speed (11 mm/s) can be the result of lack of penetration in the welded joints.
- In MAG welding, test results revealed an increase of longitudinal distortion (bending) from 1.2 to 3.6 mm when raising the heat input from 0.3 to 0.472 kJ/mm. When increases welding speed (11 mm/s), angular distortion was approximately 2.1° on the left side and 1.7° on the right side.
- For MAG welding samples, welding speed is inversely proportional to angular distortion and longitudinal distortion as well. Accordingly, heat input per unit length (kJ/mm) is proportional to angular distortion and bending. Multiplication of the heat input 1.5 times leads to an angular distortion four times worse. The best deformation result for MAG welds was found when the welding speed was 11 mm/s, and lower speeds have produced excess root penetration.
- Microstructural investigations revealed the proportionality between heat input and carbides formations on the grain boundaries of HAZ, which indicates that degree of sensitization to intergranular corrosion could be higher when heat input increases and welding speed decreases.
- The SEM analysis followed by EDS mapping scan revealed significant carbide formation on the grain boundaries when applying MAG welding processes. They were also the formation of etching pores and some ferrite content (10%) on the weld center.
- The results showed a gradient concentration of some allowing elements (Fe, Cr, Mo, Ni, and C) through the EDS spectra from the fusion line position of MAG 2 and MAG 3 samples.

## Acknowledgments

The authors would like to thank the technical support from the Cameroon Welding Association (CWA).

## Conflict of interest

The authors declare no conflict of interest.

## References

1. International Stainless Steel Forum (ISSF), Stainless steel in figures, 2020. Available from: https://www.worldstainless.org.
2. Outokumpu Oyi (2013) *Hanbook of Stainless Steel*, Finland: Outokumpu Oyi.

3. Ezer M, Cam G (2020) Investigation of the microstructure and mechanical properties of gas metal arc welded AISI 304 austenitic stainless steel butt joints, In: Çınar Ö, *2020 Proceedings of International Conference on Engineering Technology and Innovation (ICETI)*, 1–10.
4. Şenol M, Cam G (2020) Microstructural and mechanical characterization of gas metal arc welded AISI 430 ferritic stainless steel joints, In: Çınar Ö, *2020 Proceedings of International Conference on Engineering Technology and Innovation (ICETI)*, 11–19.
5. Serindağ H, Çam G (2021) Microstructure and mechanical properties of gas metal arc welded AISI 430/AISI 304 dissimilar stainless steels butt joints. *JPCS* 1777: 012047. https://doi.org/10.1088/1742-6596/1777/1/012047
6. Çam G, Yeni Ç, Erim S, et al. (1998) Investigation into properties of laser-welded similar and dissimilar steel joints. *Sci Technol Weld Joi* 3: 177-189. https://doi.org/10.1179/stw.1998.3.4.177
7. Çam G, Erim S, Yeni Ç, et al. (1999) Determination of mechanical and fracture properties of laser beam welded steel joints. *Weld J* 78: 193s-201s.
8. Çam G (2011) Friction stir welded structural materials: Beyond Al-alloys. *Int Mater Rev* 56: 1–8. https://doi.org/10.1179/095066010X12777205875750
9. Çam G, İpekoğlu G, Küçükömeroğlu T, et al. (2017) Applicability of friction stir welding to steels. *JAMME* 80: 65–85. https://doi.org/10.5604/01.3001.0010.2027
10. Yavuz H, Çam G (2005) Laser-arc hybrid welding method. *Eng and Mach* 46: 14–19.
11. Raden D, Kariem A, Neswan O, et al. (2019) Mechanical properties and microstructure at stainless steel HAZ from dissimilar metal welding after heat treatment processes. *IOP Conf Series Mater Sci Eng* 553: 012034. https://doi.org/10.1088/1757-899X/553/1/012034
12. Cao L, Shao X, Jiang P, et al. (2017) Effects of welding speed on microstructure and mechanical property of fiber laser welded dissimilar butt joints between AISI316L and EH36. *Metals* 7: 1–13. https://doi.org/10.3390/met7070270
13. Grigorenko G, Kostin A (2013) Criteria for evaluating the weldability of steels. *Weld Int* 27: 815–820. https://doi.org/10.1080/09507116.2013.796633
14. Demarque R, Dos Santos E, Silva R, et al. (2018) Evaluation of the effect of the thermal cycle on the characteristics of welded joints through the variation of the heat input of the austenitic AISI 316L steels by the GMAW process. *Sci Technology Mater* 30: 51–59. https://doi.org/10.1016/j.stmat.2018.09.001
15. Jafarzadegan M, Feng H, Abdollah-zadeh A, et al. (2012) Microstructural characterization in dissimilar friction stir welding between 304 stainless steel and st37 steel. *Mater Charact* 74: 28–41. https://doi.org/10.1016/j.matchar.2012.09.004
16. Lippold J (2014) *Welding Metallurgy and Weldability*, 1 Ed., John Wiley & Sons. https://doi.org/10.1002/9781118960332
17. Landowski M, Swierczynska A, Rogalski G, et al. (2020) Autogenous fiber laser welding of 316L austenitic and 2304 lean duplex stainless steels. *Materials* 13: 2930. https://doi.org/10.3390/ma13132930
18. Rogalski G, Swierczynska A, Landowski M, et al. (2020) Mechanical and microstructural characterization of TIG welded dissimilar joint between 304L austenitic stainless steel and Incoloy 800HT nickel alloy. *Metals* 10: 559. https://doi.org/10.3390/met10050559
19. Dong L, Zhang X, Han Y, Peng Q, et al. (2020) Effect of surface treatments on microstructure and stress corrosion cracking behaviour of 308L weld metal in a primary pressurized water reactor environment. *Corros Sci* 166: 108465. https://doi.org/10.1016/j.corsci.2020.108465

20. Kumar K, Ramkumar D, Arivazhagan N (2015) Characterization of metallurgical and mechanical properties on the multi-pass welding of Inconel 625 and AISI 316L. *J Mech Sci Technol* 29: 1039–1047. https://doi.org/10.1007/s12206-014-1112-4
21. Ramkumar D, Reddy M, Arjun R, et al. (2015) Effect of filler metals on the weldability and mechanical properties of multi-pass PCGTA weldments of AISI 316L. *J Mater Eng Perform* 24: 1602–1613. https://doi.org/10.1007/s11665-015-1418-0
22. Shankar V, Gill T, Mannan L, et al. (2003) Effect of nitrogen addition on microstructure and fusion zone cracking in type 316L stainless steel weld metals. *Mat Sci Eng A-Struct* A343: 170–181. https://doi.org/10.1016/S0921-5093(02)00377-5
23. Younes C, Steele A, Nicholson J, et al. (2013) Influence of hydrogen content on the tensile properties and fracture of austenitic stainless steel welds. *Int Hydrogen Energ* 38: 4864–4876. https://doi.org/10.1016/j.ijhydene.2012.11.016
24. Sadeghan M, Shamanian M, Shafyei A, et al. (2014) Effect of heat on microstructure and mechanical properties of dissimilar joints between super duplex stainless steel and high strength low alloy steel. *Mater Design* 60: 678–684. https://doi.org/10.1016/j.matdes.2014.03.057
25. Ramdan R, Koswara A, Wirawan R, et al. (2018) Metallurgy and mechanical properties variation with heat input, during dissimilar metal welding between stainless and carbon steel. *IOP Conf Ser Mater Sci Eng* 307: 012056. https://doi.org/10.1088/1757-899X/307/1/012056
26. Pazooki A, Hermans M, Richardson I (2017) Control of welding distortion during gas metal arc welding of AH36 plates by stress engineering. *Int Adv Manuf Tech* 88: 1439–1457. https://doi.org/10.1007/s00170-016-8869-9
27. Adamczuk P, Machado I, Mazzaferro J (2017) Methodology for predicting the angular distortion in multi-pass butt-joint welding. *J Mater Process Tech* 240: 305-313. https://doi.org/10.1016/j.jmatprotec.2016.10.006
28. Mvola B, Kah P (2017) Effects of shielding gas control: welded joint properties in GMAW process optimization. *Int Adv Manuf Tech* 88: 2369–2387. https://doi.org/10.1007/s00170-016-8936-2
29. Kaneko K, Fukunaga T, Yamada K, et al. (2011) Formation of M23C6-type precipitates and chromium-depleted zones in austenite stainless steel. *Scripta Mater* 65: 509–512. https://doi.org/10.1016/j.scriptamat.2011.06.010
30. Kozuh S, Gojic M, Kosec L (2009) Mechanical properties and microstructure of austenitic stainless after welding and post-weld heat treatment. *Kovove Mater* 47: 253–262.
31. Parvathavarthini N, Dayal R, Hhatak H, et al. (2006) Sensitization behavior of modified 316N and 316L stainless steel weld metals after complexannealing and stress relieving cycles. *J Nucl Mater* 355: 68–82. https://doi.org/10.1016/j.jnucmat.2006.04.006
32. Ghusoon R, Ishak M, Aqida S, et al. (2017) Weld bead profile of laser welding dissimilar joints stainless steel. *IOP Conf Ser Mater Sci Eng* 257: 012072 https://doi.org/10.1088/1757-899X/257/1/012072
33. Mani C, Karthikeyan R, Vincent S (2018) A study on corrosion resistance of dissimilar welds between Monel 400 and 316L austenitic steel. *IOP Conf Ser Mater Sci Eng* 346: 012025. https://doi.org/10.1088/1757-899X/346/1/012025

34. Bayock N, Kah P, Kibong M, et al. (2021) Thermal induced residual stress and microstructural constituents of dissimilar S690QT high-strength steels and 316L austenitic stainless steel weld joints. *Mater Res Express* 8: 076519. https://doi.org/10.1088/2053-1591/ac15d8


AIMS Press